MRT discrete Boltzmann method for compressible exothermic reactive flows

Chuandong Lin [a],*, Kai Hong Luo [a,b],*

[a] Center for Combustion Energy, Key Laboratory for Thermal Science and Power Engineering of Ministry of Education, Department of Energy and Power Engineering, Tsinghua University, Beijing 100084, China
[b] Department of Mechanical Engineering, University College London, Torrington Place, London WC1E 7JE, UK

ARTICLE INFO

ABSTRACT

An efficient, accurate and robust multiple-relaxation-time (MRT) discrete Boltzmann method (DBM) is proposed for compressible exothermic reactive flows, with both specific heat ratio and Prandtl number being flexible. The chemical reaction is coupled with the flow field naturally and the external force is also incorporated. An efficient discrete velocity model which has sixteen discrete velocities (and kinetic moments) is introduced into the DBM. With both hydrodynamic and thermodynamic nonequilibrium effects under consideration, the DBM provides more detailed and accurate information than traditional Navier–Stokes equations. This method is suitable for fluid flows ranging from subsonic, to supersonic and hypersonic ranges. It is validated by various benchmarks.

1. Introduction

Exothermic reactive flows are commonplace in nature and industry which play significant roles in economic and social development all over the world. In fact, more than 80% utilizable energy is transformed through exothermic reactive phenomena in the world [1]. On the other hand, they are associated with environmental problems, accidents or even disasters. For example, atmospheric pollution, global warming and climate change are closely linked to harmful emissions from reactive flows. In particular, fire hazards, which often induce explosion and shock, may cause huge danger and damage to human life, property and environment. Although considerable researches have been devoted to these fields, there are still many open issues due to their complexity. To be specific, they have a wide span of physicochemical phenomena, interact over various spatio-temporal scales, and involve various hydrodynamic and thermodynamic nonequilibrium behaviours [2–4]. Especially, for a spacecraft flying from the earth surface to outer space, where the chemical reaction and gravity exist, it covers a wide range of Knudsen numbers and various essential nonequilibrium phenomena. To describe such complex systems, traditional macroscopic models have the benefit of high computing efficiency, but could not capture detailed information accurately. While microscopic models have the merit of an accurate and full description, they encounter spatio-temporal constraints because of their high computing costs.

At the mesoscopic level, the lattice Boltzmann method (LBM) may overcome aforementioned problems [5–16]. In the past three decades, the LBM has achieved significant success in the simulation of complex systems, including reactive flows [17–35]. The traditional LBM usually works as an alternative tool to solve macroscopic equations, such as incompressible Navier–Stokes (NS) equations. Various physical quantities, such as flow velocity and temperature, may be described by different sets of the discrete distribution function. Recently, a novel variant of LBM, discrete Boltzmann method (DBM), has emerged as an efficient kinetic model to capture both hydrodynamic and thermodynamic nonequilibrium effects in fluid flows [36,37]. Different from traditional LBMs, the DBM employs only one set of discrete distribution function to describe various physical quantities, including the density, temperature, velocity, and other high order kinetic moments, which is in line with the Boltzmann equation.

* Corresponding authors.
E-mail addresses: chuandonglin@163.com (C. Lin), K.Luo@ucl.ac.uk (K.H. Luo).
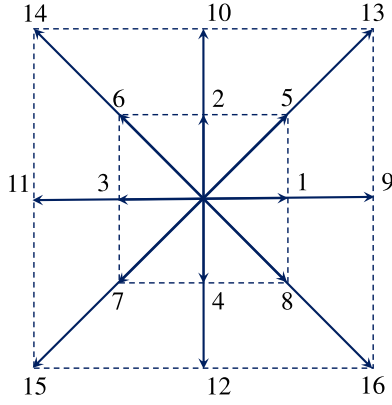
Fig. 1. Sketch of the discrete velocity model D2V16.

Since 2013, several Single-Relaxation-Time DBMs have been formulated for exothermic reactive flows [38–40]. Yet, the Prandtl number in those proposed model is fixed at Pr = 1. To overcome this, a multiple-relaxation-time (MRT) DBM was presented [41]. There are 24 independent kinetic moments satisfied by 24 discrete equilibrium distribution functions in this work [41]. These kinetic moments are necessary for the DBM to recover the reactive NS equations in the hydrodynamic limit [41]. Besides, the effects of external force are neglected in this model [41]. However, external forces (such as gravity) often have essential influences upon reactive flows. In the present work, we introduce a new form of reaction and force terms, and reduce the 24 kinetic moments (and discrete equilibrium distribution functions) to only 16 while the recovery of the NS equations is made as well. Besides its practical value as an efficient computational tool for the traditional dynamics of complex systems, this model also provides details of nonequilibrium behaviours dynamically and conveniently. We describe the DBM in Section 2, validate it in Section 3, and finally summarize this work in Section 4.

2. Discrete Boltzmann method

The DBE takes the form,

$$\frac{\partial \mathbf{f}}{\partial t} + \mathbf{v} \cdot \nabla \mathbf{f} = -\mathbf{M}^{-1}\hat{\mathbf{S}}\left(\hat{\mathbf{f}} - \hat{\mathbf{f}}^{eq}\right) - \mathbf{A} + \mathbf{F} + \mathbf{R}. \tag{1}$$

Here $\mathbf{f} = (f_1\ f_2\ \cdots\ f_N)^{\mathrm{T}}$ and $\mathbf{f}^{eq} = (f_1^{eq}\ f_2^{eq}\ \cdots\ f_N^{eq})^{\mathrm{T}}$ denote discrete distribution functions and their equilibrium counterparts, respectively. $\hat{\mathbf{f}} = (\hat{f}_1\ \hat{f}_2\ \cdots\ \hat{f}_N)^{\mathrm{T}}$ and $\hat{\mathbf{f}}^{eq} = (\hat{f}_1^{eq}\ \hat{f}_2^{eq}\ \cdots\ \hat{f}_N^{eq})^{\mathrm{T}}$ represent kinetic moments of discrete distribution function and their equilibrium counterparts, respectively. $\mathbf{M}^{-1}$ is the inverse matrix of $\mathbf{M}$, and $\mathbf{M}$ is a square matrix, see Appendix A. $\hat{\mathbf{S}} = \mathrm{diag}(\hat{S}_1\ \hat{S}_2\ \cdots\ \hat{S}_N)$ is a diagonal matrix with element $\hat{S}_i$ describing the speed of $\hat{f}_i$ approaching $\hat{f}_i^{eq}$, with $i = 1, 2, \cdots, N$ and $N = 16$. As shown in Fig. 1, the discrete velocities, $\mathbf{v} = \mathrm{diag}(\mathbf{v}_1\ \mathbf{v}_2 \cdots \mathbf{v}_N)$, take the following form,

$$\mathbf{v}_i = \begin{cases} \mathrm{cyc} : (\pm v_a, 0) & 1 \le i \le 4, \\ \mathrm{cyc} : (\pm v_a, \pm v_a) & 5 \le i \le 8, \\ \mathrm{cyc} : (\pm v_b, 0) & 9 \le i \le 12, \\ \mathrm{cyc} : (\pm v_b, \pm v_b) & 13 \le i \le 16, \end{cases} \tag{2}$$

with tunable parameters v_a and v_b controlling the value of $\mathbf{v}_i$.

The artificial term $\hat{\mathbf{A}} = (0\ \cdots\ 0\ \hat{A}_8\ \hat{A}_9\ 0\ \cdots\ 0)^{\mathrm{T}}$ is used to modify the collision operator $\mathbf{\Omega} = -\mathbf{M}^{-1}\hat{\mathbf{S}}(\hat{\mathbf{f}} - \hat{\mathbf{f}}^{eq})$, in terms of

$$\hat{A}_8 = \rho T \frac{\hat{S}_8 - \hat{S}_5}{\hat{S}_5}\left[4u_x\left(\frac{D+I-1}{D+I}\frac{\partial u_x}{\partial x} - \frac{1}{D+I}\frac{\partial u_y}{\partial y}\right)\right.$$
$$\left. + 2u_y\left(\frac{\partial u_y}{\partial x} + \frac{\partial u_x}{\partial y}\right)\right], \tag{3}$$

$$\hat{A}_9 = \rho T \frac{\hat{S}_9 - \hat{S}_7}{\hat{S}_7}\left[4u_y\left(\frac{D+I-1}{D+I}\frac{\partial u_y}{\partial y} - \frac{1}{D+I}\frac{\partial u_x}{\partial x}\right)\right.$$
$$\left. + 2u_x\left(\frac{\partial u_y}{\partial x} + \frac{\partial u_x}{\partial y}\right)\right]. \tag{4}$$

The reason for this modification is as follows. Although the tunable relaxation coefficients $\hat{S}_i$ seem mathematically independent of each other, coupling may exist among the relaxation processes of various kinetic modes ($\hat{f}_i^{ne} = \hat{f}_i - \hat{f}_i^{eq}$) from the physical point of view. For the sake of correct description of macroscopic behaviours, we should perform the Chapman–Enskog expansion, analyze the consistency of nonequilibrium transportation terms in the recovered hydrodynamic equations, and find a solution for the modification to the collision term. In short, this modification is incorporated in the DBM to recover the consistent NS equations in the hydrodynamic limit, see Appendix A. The artificial term is the function of the velocities (u_x, u_y) and the first-order partial derivatives of them with respect to x or y. These derivatives can be solved by various finite difference schemes. In this work, the central difference scheme is adopted. For example,

$$\frac{\partial u_x}{\partial x} = \frac{u_x(i_x + 1, i_y) - u_x(i_x - 1, i_y)}{2\Delta x} \tag{5}$$

at the node (i_x, i_y). Numerical tests demonstrate that the artificial term does not induce significant numerical problems. Furthermore, the artificial term can be removed for the case $\hat{S}_5 = \hat{S}_8$ and $\hat{S}_7 = \hat{S}_9$.

The force and reaction terms, $\mathbf{F} + \mathbf{R} = (F_1 + R_1\ F_2 + R_2\ \cdots\ F_N + R_N)^{\mathrm{T}}$, describe the variations of the distribution function due to the external force and chemical reaction. Specifically,

$$F_i + R_i = \frac{1}{\tau}\left[f_i^{eq}(\rho, \mathbf{u} + \mathbf{a}\tau, T + \tau T') - f_i^{eq}(\rho, \mathbf{u}, T)\right]. \tag{6}$$

Mathematically, the difference of the equilibrium distribution functions over a small time interval is an approximation to the change rate of distribution functions, based on the assumption $f_i \approx f_i^{eq}$. The physical reason for Eq. (6) is as follows. It is regarded that neither external force nor chemical reaction changes the density ρ. The external force affects the hydrodynamic velocity $\mathbf{u}$ with acceleration $\mathbf{a}$. Consequently, the velocity changes from $\mathbf{u}$ into $\mathbf{u} + \mathbf{a}\tau$ within a small time interval τ due to the external force. Meanwhile, the temperature changes into $T + \tau T'$ on account of the chemical reaction. Specifically, the change rate of energy is

$$E' = \rho\mathbf{u} \cdot \mathbf{a} + \rho Q\lambda', \tag{7}$$

because of the external force and chemical reaction. From Eq. (7) and the definition $E = \frac{D+I}{2}\rho T + \frac{1}{2}\rho\mathbf{u} \cdot \mathbf{u}$, we obtain the change rate of temperature

$$T' = \frac{2Q\lambda'}{D+I}, \tag{8}$$

where $D = 2$ stands for the number of dimensions, I the number of extra degrees of freedom corresponding to molecular rotation and/or internal vibration. The reaction process λ is defined as the mass ratio of the chemical product to mixture. The chemical reaction is controlled by the Cochran's rate function

$$\lambda' = \omega_1 p^m(1 - \lambda) + \omega_2 p^n\lambda(1 - \lambda), \tag{9}$$

which depends upon the pressure, $p = \rho T$, in terms of adjustable parameters ω_1, ω_2, m and n [42]. Here λ is defined as the local mass fraction of the reaction product. Without loss of generality, we choose (ω_1, ω_2, m, n) = (2, 100, 2, 2.5), and employ the ignition temperature $T_{ig} = 1.1$ in this work. Only when $T > T_{ig}$ can the chemical reaction take place.

For the sake of recovering the NS equations, the discrete equilibrium distribution function should satisfy the following relations

$$\sum f_i^{eq} = \rho, \tag{10}$$

$$\sum f_i^{eq} v_{i\alpha} = \rho u_\alpha, \tag{11}$$

$$\sum f_i^{eq} (v_i^2 + \eta_i^2) = \rho[(D+I)T + u^2], \tag{12}$$

$$\sum f_i^{eq} v_{i\alpha} v_{i\beta} = \rho(\delta_{\alpha\beta}T + u_\alpha u_\beta), \tag{13}$$

$$\sum f_i^{eq} (v_i^2 + \eta_i^2) v_{i\alpha} = \rho u_\alpha[(D+I+2)T + u^2], \tag{14}$$

$$\sum f_i^{eq} v_{i\alpha} v_{i\beta} v_{i\chi} = \rho(u_\alpha \delta_{\beta\chi} + u_\beta \delta_{\chi\alpha} + u_\chi \delta_{\alpha\beta})T + \rho u_\alpha u_\beta u_\chi, \tag{15}$$

$$\sum f_i^{eq} (v_i^2 + \eta_i^2) v_{i\alpha} v_{i\beta} = \rho \delta_{\alpha\beta}[(D+I+2)T + u^2]T$$
$$+ \rho u_\alpha u_\beta[(D+I+4)T + u^2], \tag{16}$$

where η_i^2 is employed to describe internal energies in extra degrees of freedom, with $\eta_i = \eta_a$ for $5 \leq i \leq 8$ and $\eta_i = 0$ for the others.

In fact, Eqs. (10)–(16) can be uniformly written as $\mathbf{M} \times \mathbf{f}^{eq} = \hat{\mathbf{f}}^{eq}$. In Eqs. (10)–(12), f_i^{eq} can be replaced by f_i, from which we can calculate physical quantities (ρ, $\mathbf{u}$, T). Whereas replacing f_i^{eq} with f_i results in the imbalance between the left and right sides of Eqs. (13)–(16). These differences are just departures of high order kinetic moments of the distribution function from their equilibrium counterparts, i.e., $\hat{f}_i^{ne} = \hat{f}_i - \hat{f}_i^{eq}$. The departures can be utilized to probe the nonequilibrium states from various points of view. Note that $\hat{f}_i^{ne} = 0$ for $1 \leq i \leq 4$ due to the conservation laws, hence the parameters $\hat{S}_1$, $\hat{S}_2$, $\hat{S}_3$ and $\hat{S}_4$ do not play any role. While $\hat{f}_i^{ne}$ may be nonzero for $i \geq 5$ in nonequilibrium state. To be specific, $\hat{f}_5^{ne}$ ($\hat{f}_7^{ne}$) is the departure of energy in the x (y) direction from its equilibrium state; $\hat{f}_5^{ne}$, $\hat{f}_6^{ne}$, and $\hat{f}_7^{ne}$ are linked with the viscous stress tensor; $\hat{f}_8^{ne}$, $\hat{f}_9^{ne}$, $\hat{f}_{10}^{ne}$, $\hat{f}_{11}^{ne}$, $\hat{f}_{12}^{ne}$, and $\hat{f}_{13}^{ne}$ refer to the departures of energy fluxes from their equilibrium counterparts; $\hat{f}_{14}^{ne}$, $\hat{f}_{15}^{ne}$, and $\hat{f}_{16}^{ne}$ are related to fluxes of energy flux from their equilibrium counterparts. The nonequilibrium effect $\hat{f}_i^{ne}$, multiplied by its amplification factor $\hat{S}_i$, plays an essential role in the evolution of fluid systems. It is clear that $\hat{f}_i^{ne}$ in Eq. (A.1) has a strong effect with large $\hat{S}_i$. Actually, those departures are calculated conveniently in each iteration of the computing process. Moreover, the dynamic viscosity μ, thermal conductivity κ, and Prandtl number Pr are functions of $\hat{S}_i$. Specifically, $\mu = \rho T / \hat{S}_\mu$, $\kappa = (D+I+2)\rho T/(2\hat{S}_\kappa)$, and Pr $= \hat{S}_\kappa / \hat{S}_\mu$, for $\hat{S}_\mu = \hat{S}_5 = \hat{S}_6 = \hat{S}_7$ and $\hat{S}_\kappa = \hat{S}_8 = \hat{S}_9$, see Appendix A. In contrast, all the amplification factors are identical in the SRT model, i.e., Pr $= 1$, which is only a special case of the MRT model.

It can be found that discrete Boltzmann equation is in a simple form and its algorithm is easy to code. In contrast, the NS equations depend upon both the first-order and second-order partial derivatives of velocities (u_x, u_y) with respect to x or y, which are nonlinear terms relatively difficult to be treated with [40]. Moreover, it often needs to solve the Poisson equation based on global data transfer in NS method, while all spatio-temporal information communication is local in DBM that is suitable for massively parallel computing. In addition, the DBM provides an efficient tool to study detailed nonequilibrium effects and/or rarefied effects of gas flows beyond NS equations by capturing the departures of kinetic moments from their equilibrium counterparts [40,43]. Finally, it is
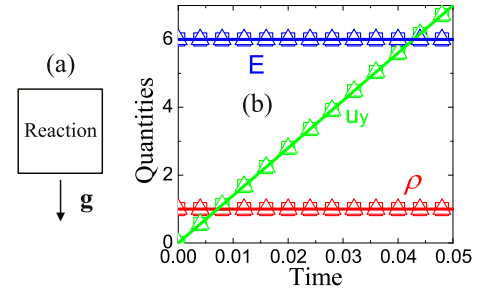

Fig. 2. Initial configuration (a) and time evolution (b) of physical quantities in the process of chemical reaction in a free falling box. The squares stand for D2V16 results, triangles for D2V24 results, and lines for exact solutions.

easy to have a proper kinetic boundary condition for DBM to describe the velocity slip and the flow characteristics in the Knudsen layer that cannot be well described by traditional hydrodynamic models [43].

3. Validation and verification

For validation and verification purposes, four benchmark tests are performed. (i) The chemical reaction in a free falling box is simulated to verify the effects of external force and chemical reaction. (ii) The simulation of a detonation wave is carried out to demonstrate the DBM in the case with violent chemical heat release. Additionally, we assess the spatial and temporal convergence of the numerical results. (iii) To verify the DBM for adjustable specific heat ratios and Prandtl numbers, we simulate Couette flow. Moreover, it is demonstrated that the nonequilibrium information provided by the DBM coincides with its analytical solution. (iv) Finally, a typical two-dimensional benchmark, shock reflection, is simulated successfully. Besides, it is demonstrated in the first two tests that the discrete velocity model D2V16 has higher efficiency and better robustness than D2V24 [41]. Note that the second order Runge–Kutta scheme is adopted for the time derivative, while the second order nonoscillatory and nonfree-parameter dissipation difference scheme [44] is employed for the space derivative in Eq. (1). It is preferable to set $\Delta t \leq 1/\text{Max}(\hat{S}_i)$ due to the explicit scheme for the time derivative, where $\text{Max}(\hat{S}_i)$ denotes the maximum among $\hat{S}_i$. The relation between the time step Δt and space step $\Delta x = \Delta y$ should satisfy convergence conditions. Additionally, variables and parameters used in this paper are expressed in nondimensional forms, i.e., the widely accepted LB units [45,46].

3.1. Reaction in a free falling box

First of all, we simulate the exothermic chemical reaction in a free falling box, see Fig. 2(a). Initially, the box is evenly filled with premixed chemical reaction with released heat $Q = 1.0$, density $\rho = 1.0$, temperature $T = 2.0$, velocity $\mathbf{u} = 0$, and acceleration $\mathbf{g} = (0, 140)$. The reaction is ignited uniformly, hence we adopt only one mesh grid, i.e., $N_x = N_y = 1$, and the space step $\Delta x = \Delta y = 10^{-5}$, time step $\Delta t = 10^{-6}$. In addition, the specular reflection boundary conditions are imposed. There are two purposes of this simulation. One is to validate the simulation results in the case with both the external force and chemical reaction taken into account. The other is to compare D2V16 with D2V24 constructed in Ref. [41]. The parameters $(v_a, v_b, \eta_a) = (1.7, 3.7, 3.3)$ is adopted for D2V16, and $(v_a, v_b, v_c, \eta_a, \eta_b, \eta_c) = (1.2, 1.9, 2.7, 3.5, 0.1, 2.0)$ is chosen for D2V24. For both D2V16 and D2V24 models, the collision parameters are $\hat{S}_i = 10^5$ except $\hat{S}_5 = \hat{S}_6 = \hat{S}_7 = 2 \times 10^4$. Correspondingly, the Prandtl number Pr $= \hat{S}_\kappa / \hat{S}_\mu = 5$, with $\hat{S}_\mu = \hat{S}_5 = \hat{S}_6 = \hat{S}_7$, and $\hat{S}_\kappa = \hat{S}_8 = \hat{S}_9$. The specific heat ratio is $\gamma = (I+4)/(I+2) = 1.4$.
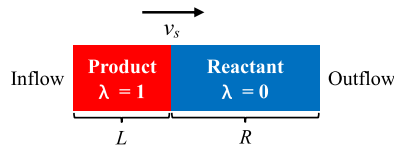
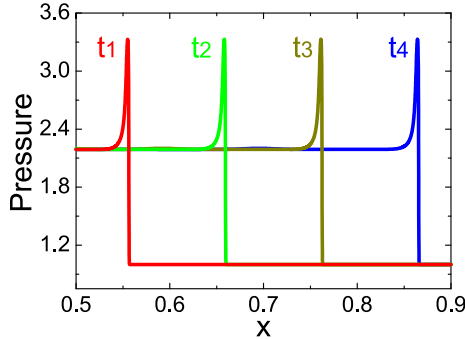**Fig. 3.** Sketch of the initial configuration for detonation.

Fig. 4. Pressure profiles in the evolution of the detonation wave at times, $t_1 = 0.25$, $t_2 = 0.30$, $t_3 = 0.35$, and $t_4 = 0.40$, respectively.

Fig. 2(b) displays the evolution of physical quantities (ρ, u_y, E), where E is the sum of internal energy and chemical heat. The squares are for D2V16 results, triangles for D2V24 results, and lines for exact solutions. In the process of chemical reaction in the free falling box, the chemical reactant changes into the product and the chemical heat is released, with the conservation of total mass, momentum and energy. Obviously, both D2V16 and D2V24 provide numerical results $\rho = 1.0$ and $E = 6.0$, which equal the exact solutions precisely. And the flow velocity simulated by either D2V16 or D2V24 coincides the exact $\mathbf{u} = \mathbf{g}t$. Consequently, both D2V16 and D2V24 are satisfactory. Moreover, on a personal computer, the computing time is 1.3 s for D2V16, and 2.4 s for D2V24. Clearly, D2V16 requires less RAM and shorter computing time than D2V24.

3.2. Detonation wave

In order to test the present DBM under the condition with violet chemical heat release, we target the detonation wave. The initial configuration is

$$\begin{cases} (\rho, T, u_x, u_y, \lambda)_L = (1.38837, 1.57856, 0.57735, 0, 1) \\ (\rho, T, u_x, u_y, \lambda)_R = (1, 1, 0, 0, 0) \end{cases} \quad (17)$$

where the suffix L indexes the left part, $0 \le x \le 0.05$, and R the right part $0.05 < x \le 1$, see Fig. 3. The inflow or outflow condition is adopted in the x direction, the period condition is employed in the y direction. The parameters are $I = 3$, $Q = 1$, $(v_a, v_b, \eta_a) = (1.7, 3.7, 3.3)$, $\Delta t = 10^{-5}$, $\Delta x = \Delta y = 10^{-4}$, and $N_x \times N_y = 10,000 \times 1$. The collision parameters are $\hat{S}_i = 10^5$ except $\hat{S}_\mu$ (i.e., $\hat{S}_5$, $\hat{S}_6$, $\hat{S}_7$) $= 2 \times 10^4$.

The detonation wave travels from left to right with speed v_s. The chemical reactant is in front of the detonation wave with $\lambda = 0$, and it changes into the product after the wave with $\lambda = 1$. Fig. 4 illustrates the propagation of pressure at time instants, $t_1 = 0.25$, $t_2 = 0.30$, $t_3 = 0.35$, and $t_4 = 0.40$, respectively. It can be obtained in Fig. 4 that the speed of the detonation wave is $v_s = 2.062$. Compared with the theoretical value $v_s = 2.06395$, the error is only 0.09%, which is satisfactory.

The physical quantities (ρ, u_x, T, p) firstly increase in the compression zone, then reduce in the rarefaction zone, and finally level off after the detonation wave. Their profiles at time $t_4 = 0.40$ are plotted in Fig. 5 (a)–(d). Squares are for numerical results and lines are for Zeldovich–Neumann–Doering (ZND) solutions [2]. Simulation results behind the detonation wave are (ρ, u_x, T, p) = (1.38907, 0.577593, 1.57737, 2.19109). Compared with the analytical solutions (ρ, u_x, T, p) = (1.38837, 0.57735, 1.57856, 2.19162), the relative differences are (0.05%, 0.04%, 0.08%, 0.02%), respectively. Obviously, the numerical and analytical results coincide well in Fig. 5. The tiny differences between them are due to the fact that the ZND theory ignores the viscosity and heat conduction, and the von Neumann peak is assumed as a strong discontinuity which is not a truth. The DBM considers the viscosity, heat conduction as well as other nonequilibrium effects. Note that, with the decrease of collision parameters, the nonequilibrium effects are enhanced, and the differences between the DBM and analytical solutions become large [41].

To compare the numerical robustness of D2V16 and D2V24 [41], the aforementioned detonation wave is simulated by using the D2V24 as well. The parameters are $(v_a, v_b, v_c, \eta_a, \eta_b, \eta_c) = (3.5, 4.0, 5.0, 4.0, 0.0, 3.0)$ for D2V24. The other parameters are the same as those for D2V16. Fig. 6 exhibits the pressure profile at time $t = 0.028$. The solid (dotted) line stands for D2V16 (D2V24).
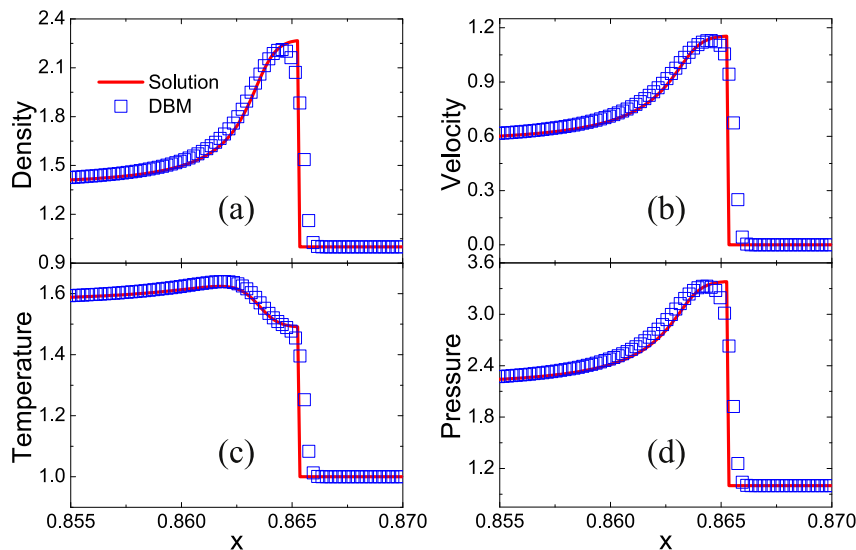

Fig. 5. Profiles of the detonation wave: (a) density ρ, (b) velocity u_x, (c) temperature T, and (d) pressure p. Squares and lines refer to numerical and analytical results, respectively
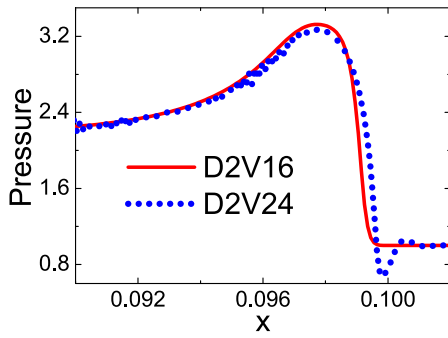
Fig. 6. Comparison between simulation results of D2V16 and D2V24.

Obviously, D2V16 gives a smooth profile around the detonation front, while D2V24 gives an oscillating profile. This nonphysical oscillation is soon amplified and results in the stop of the simulation program. Moreover, further tests demonstrate that D2V16 is capable of simulating the detonation wave for Mach number Ma > 100. However, it is difficult and even impossible to use D2V24 to simulate such high-Mach systems.

Next, let us assess the spatial and temporal convergence of the DBM results. The spatial convergence is proved considering several values of the space step, $\Delta x = \Delta y = 5 \times 10^{-6}$, 1×10^{-5}, 2×10^{-5}, 4×10^{-5}, 8×10^{-5}, 1.6×10^{-4}, with fixed time step $\Delta t = 1 \times 10^{-6}$. The relative difference of the minimum value of $\hat{f}_5^{ne}$ around the detonation wave is chosen as the numerical error. Fig. 7 (a) illustrates the numerical error versus space step. The squares stand for the DBM results and the line for the fitting function, ln(error) = $k \ln(\Delta x) + 10.2446$, with the slope $k = 2.16164$. It is near the exact value $k = 2$ since the space derivative is solved at the second order level.

In a similar way, the temporal convergence is demonstrated considering several values of the time step, $\Delta t = 5 \times 10^{-7}$, 1×10^{-6}, 2×10^{-6}, 4×10^{-6}, 8×10^{-6}, 1.6×10^{-5}, with fixed space step $\Delta x = \Delta y = 1.6 \times 10^{-4}$. Fig. 7 (a) illustrates the numerical error versus time step. The fitting function takes the form, ln(error) = $k \ln(\Delta t) + 15.6137$ with $k = 2.06822$. The slope is close to the exact one $k = 2$ because the second order scheme is used for the time derivative.

3.3. Couette flow

To verify the DBM for various values of the specific heat ratio γ and Prandtl number Pr, we simulate Couette flow. The velocities of the upper and lower walls are $\mathbf{u} = u_0 \mathbf{e}_x$ and 0, respectively. Here $\mathbf{e}_x$ is the unit vector in the x direction, and $u_0 = 0.1$. The distance between the two walls is $H = 0.2$. The initial flow field is set as $(\rho, \mathbf{u}, T) = (1, 0, 1)$. The viscous shear stress transmits momentum into the fluid and changes the flow velocity distribution, see Fig. 10.
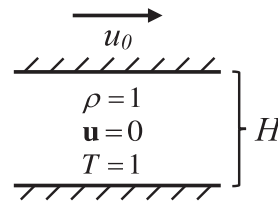

Fig. 8. Sketch of the initial configuration for Couette flow.

When the field reaches steady, the temperature is different for various γ or Pr, see Fig. 9. The space step is $\Delta x = \Delta y = 10^{-3}$, the time step $\Delta t = 5 \times 10^{-5}$, and the parameters $(v_a, v_b, \eta_a) = (1.1, 1.7, 2.3)$. Periodic boundary conditions are employed for the left and right boundaries, and the nonequilibrium extrapolation method is applied to the top and bottom boundaries. The sketch of the initial configuration for Couette flow is shown in Fig. 8.

Fig. 9 illustrates the temperature T versus y when the Couette flow reaches equilibrium. Fig. 9(a) shows the cases with $\gamma = 1.3$, 1.5, 1.8, and fixed Pr = 1.0; Fig. 9(b) shows the cases with Pr = 0.5, 1.0, 2.0, and fixed $\gamma = 1.5$. The collision parameter $\hat{S}_\mu$ is 2×10^3 for Pr = 0.5, 1×10^3 for Pr = 1.0, and 5×10^2 for Pr = 2.0, the other collision parameters $\hat{S}_i$ are 1×10^3. The symbols represent DBM results, the lines denote the corresponding analytical solutions,

$$T = T_1 + (T_2 - T_1)\frac{x}{H} + \frac{\mu}{2\kappa}u_0^2\frac{x}{H}\left(1 - \frac{x}{H}\right), \tag{18}$$

where $T_1(= 1.0)$ and $T_2(= 1.0)$ are temperatures of the lower and upper walls, respectively. Obviously, the numerical results agree well with the analytical solutions. Fig. 10 exhibits the horizontal velocity u_x (a) and nonequilibrium quantity $\hat{f}_6^{ne}$ (b) versus y in the case with $\gamma = 1.5$ and Pr = 0.5. The squares, circles, triangles, and diamonds stand for DBM results at times $t_1 = 0.05$, $t_2 = 1$, $t_3 = 5$, and $t_4 = 30$, respectively. In panel (a), the lines are for the analytical solutions,

$$u = \frac{y}{H}u_0 + \frac{2}{\pi}u_0\sum_{n=1}^{\infty}\left[\frac{(-1)^n}{n}exp\left(-n^2\pi^2\frac{\mu t}{\rho H^2}\right)sin\left(\frac{n\pi y}{H}\right)\right]. \tag{19}$$

Clearly, the numerical and analytical results coincide well with each other. Hence, the DBM has the capability of capturing the flow field in the dynamic process of the Couette Flow. In panel (b), the lines stand for the analytical solutions

$$\hat{f}_6^{ne} = -\mu\left(\frac{\partial u_x}{\partial y} + \frac{\partial u_y}{\partial x}\right). \tag{20}$$

It can be found that the DBM results are in good agreement with the analytical values. That is to say, the DBM could describe the nonequilibrium behaviours accurately.
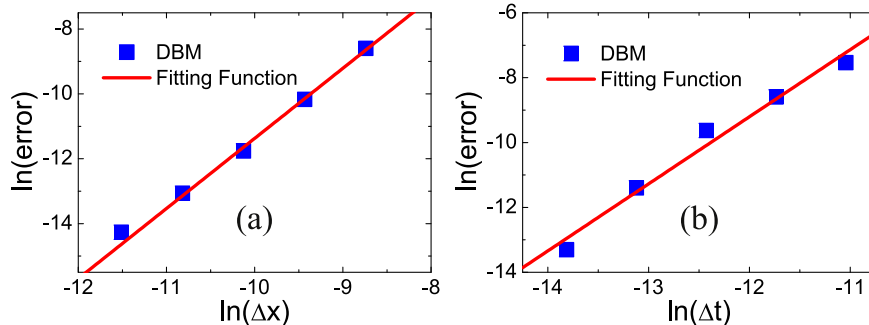

Fig. 7. Numerical errors versus space (a) and time steps (b). The squares stand for the DBM results and the line for the fitting function.
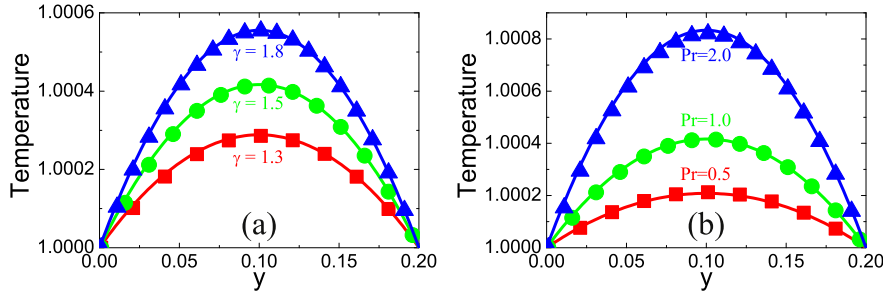
Fig. 9. Temperature distribution of steady Couette flow: (a) $\gamma = 1.3$ (squares), 1.5 (circles), 1.8 (triangles), and fixed Pr = 1.0, (b) Pr = 0.5 (squares), 1.0 (circles), 2.0 (triangles), and fixed $\gamma = 1.5$. The symbols indicate DBM results and the lines denote analytical solutions.
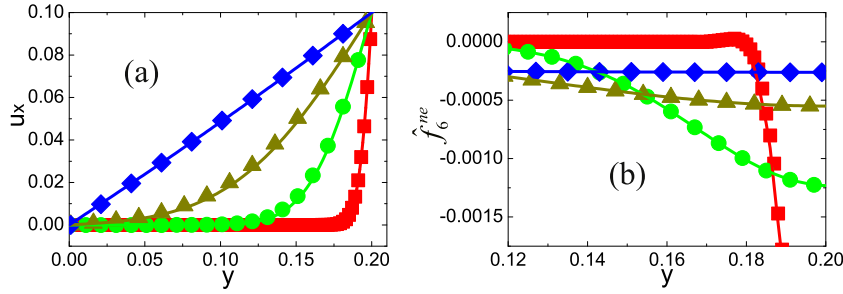

Fig. 10. Distribution of u_x (a) and $\hat{f}_6^{ne}$ (b) along y in the evolution of Couette flow at various times: $t_1 = 0.05$ (squares), $t_2 = 1$ (circles), $t_3 = 5$ (triangles), and $t_4 = 30$ (diamonds), respectively. The symbols stand for numerical results, the lines for analytical solutions.
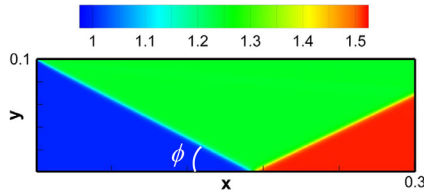

Fig. 11. Density contour of steady regular shock reflection on a wall.

3.4. Shock reflection

For the purpose of verifying the model for two dimensional systems, we use a typical benchmark: regular shock reflection. The computational domain is a rectangle. The reflecting surface is imposed on the bottom, the supersonic outflow is adopted for the right boundary, and the Dirichlet conditions are utilized on the top and left boundaries, i.e.,

$$\begin{cases} (\rho, T, u_x, u_y)_{0,y,t} = (1, 0.5, 2, 0) \\ (\rho, T, u_x, u_y)_{x,0.1,t} = (1.25, 0.56, 1.9, -0.173205) \end{cases} \quad (21)$$

The interesting readers refer to Ref. [41] for more details of the initial configuration. The parameters are $N_x \times N_y = 300 \times 100$, $\Delta x = \Delta y = 10^{-3}$, $\Delta t = 5 \times 10^{-6}$, $I = 2$, $(v_a, v_b, \eta_a) = (1.7, 2.9, 3.0)$. The collision parameters are $\hat{S}_\mu = 1.8 \times 10^5$, and 2×10^5 for the others. Fig. 11 exhibits the density contour of the steady regular shock reflection. Theoretically, the angle between the incident shock wave and the wall is $\phi = \pi/6$ while the DBM gives the angle $\phi = \text{ArcTan}(0.1/0.173)$. The relative difference between them is only 0.1%, which is satisfying.

4. Conclusions

We present an MRT DBM for compressible flows, taking both chemical reaction and external force into account. The specific heat ratio as well as the Prandtl number are flexible. This model recovers the reactive NS equations in the hydrodynamic limit.

Meanwhile, thermodynamic nonequilibrium effects are dynamically taken into account through considering the departures of kinetic moments from their equilibrium counterparts. In fact, the nonequilibrium effects together with their relaxation parameters play a crucial role in fluid systems.

Compared with a previous MRT DBM where 24 discrete velocities (and kinetic moments) are employed to couple the chemical reaction with fluid flows [41], our model requires only 16 discrete velocities (and kinetic moments) and thus less computing efforts. Compared to another MRT DBM with the incorporation of only a conventional force term [37], our model introduces a new form for both force and reaction terms, which are physically more general. In this paper, we also demonstrate that the present model provides high computational efficiency, physical fidelity, and numerical robustness

Appendix A

The elements of matrix $\mathbf{f}^{eq}$ take the form $\hat{f}_1^{eq} = \rho$, $\hat{f}_2^{eq} = \rho u_x$, $\hat{f}_3^{eq} = \rho u_y$, $\hat{f}_4^{eq} = \rho[(D+I)T + u^2]$, $\hat{f}_5^{eq} = \rho(T + u_x^2)$, $\hat{f}_6^{eq} = \rho u_x u_y$, $\hat{f}_7^{eq} = \rho(T + u_y^2)$, $\hat{f}_8^{eq} = \rho u_x[(D+I+2)T + u^2]$, $\hat{f}_9^{eq} = \rho u_y[(D+I+2)T + u^2]$, $\hat{f}_{10}^{eq} = 3\rho u_x T + \rho u_x^3$, $\hat{f}_{11}^{eq} = \rho u_y T + \rho u_x^2 u_y$, $\hat{f}_{12}^{eq} = \rho u_x T + \rho u_x u_y^2$, $\hat{f}_{13}^{eq} = 3\rho u_y T + \rho u_y^3$, $\hat{f}_{14}^{eq} = \rho[(D+I+2)T + u^2] + \rho u_x^2[(D+I+4)T + u^2]$, $\hat{f}_{15}^{eq} = \rho u_x u_y[(D+I+4)T + u^2]$, $\hat{f}_{16}^{eq} = \rho[(D+I+2)T + u^2] + \rho u_y^2[(D+I+4)T + u^2]$. The elements

of matrix $\mathbf{M}$ read $M_{1i} = 1$, $M_{2i} = v_{ix}$, $M_{3i} = v_{iy}$, $M_{4i} = v_i^2 + \eta_i^2$, $M_{5i} = v_{ix}^2$, $M_{6i} = v_{ix}v_{iy}$, $M_{7i} = v_{iy}^2$, $M_{8i} = (v_i^2 + \eta_i^2)v_{ix}$, $M_{9i} = (v_i^2 + \eta_i^2)v_{iy}$, $M_{10i} = v_{ix}^3$, $M_{11i} = v_{ix}^2 v_{iy}$, $M_{12i} = v_{ix}v_{iy}^2$, $M_{13i} = v_{iy}^3$, $M_{14i} = (v_i^2 + \eta_i^2)v_{ix}^2$, $M_{15i} = (v_i^2 + \eta_i^2)v_{ix}v_{iy}$, $M_{16i} = (v_i^2 + \eta_i^2)v_{iy}^2$.

Let us introduce quantities $\hat{\mathbf{E}} = \mathbf{MvM}^{-1}$, $\hat{\mathbf{f}} = \mathbf{Mf}$, $\hat{\mathbf{A}} = \mathbf{MA}$, $\hat{\mathbf{F}} = \mathbf{MF}$, $\hat{\mathbf{R}} = \mathbf{MR}$. Then the first nine elements of $\hat{\mathbf{F}}$ and $\hat{\mathbf{R}}$ are obtained, i.e., $\hat{F}_1 = 0$, $\hat{F}_2 = \rho a_x$, $\hat{F}_3 = \rho a_y$, $\hat{F}_4 = 2\rho u_x a_x + 2\rho u_y a_y$, $\hat{F}_5 = 2\rho u_x a_x$, $\hat{F}_6 = \rho u_x a_y + \rho u_y a_x$, $\hat{F}_7 = 2\rho u_y a_y$, $\hat{F}_8 = 2\rho u_x(u_x a_x + u_y a_y) + \rho a_x u^2 + \rho a_x(D + I + 2)T$, $\hat{F}_9 = 2\rho u_y(u_x a_x + u_y a_y) + \rho a_y u^2 + \rho a_y(D + I + 2)T$, $\hat{R}_1 = 0$, $\hat{R}_2 = 0$, $\hat{R}_3 = 0$, $\hat{R}_4 = 2\rho\lambda'Q$, $\hat{R}_5 = \rho\frac{2\lambda'Q}{D+I}$, $\hat{R}_6 = 0$, $\hat{R}_7 = \rho\frac{2\lambda'Q}{D+I}$, $\hat{R}_8 = (D + I + 2)\rho u_x\frac{2\lambda'Q}{D+I}$, $\hat{R}_9 = (D + I + 2)\rho u_y\frac{2\lambda'Q}{D+I}$, which are necessary in the following Chapman-Enskog analysis.

Multiplying Eq. (1) by $\mathbf{M}$ leads to

$$\frac{\partial\hat{\mathbf{f}}}{\partial t} + \nabla\cdot\left(\hat{\mathbf{E}}\hat{\mathbf{f}}\right) = -\hat{\mathbf{S}}\left(\hat{\mathbf{f}} - \hat{\mathbf{f}}^{eq}\right) - \hat{\mathbf{A}} + \hat{\mathbf{F}} + \hat{\mathbf{R}}, \tag{A.1}$$

Substituting the variables' expansion,

$$\begin{cases} \hat{f}_i = \hat{f}_i^{(0)} + \hat{f}_i^{(1)} + \hat{f}_i^{(2)} + \cdots \\ \frac{\partial}{\partial t} = \frac{\partial}{\partial t_1} + \frac{\partial}{\partial t_2} + \cdots \\ \nabla = \nabla_1 \Leftrightarrow \frac{\partial}{\partial r_\alpha} = \frac{\partial}{\partial r_{1\alpha}} \\ \hat{A}_i = \hat{A}_{1i}, \ \hat{F}_i = \hat{F}_{1i}, \ \hat{R}_i = \hat{R}_{1i}, \end{cases} \tag{A.2}$$

into Eq. (A.1) gives

$$\hat{\mathbf{f}}^{(0)} = \hat{\mathbf{f}}^{eq}, \tag{A.3}$$

$$\left(\frac{\partial}{\partial t_1} + \hat{\mathbf{E}}\cdot\nabla_1\right)\hat{\mathbf{f}}^{(0)} = -\hat{\mathbf{S}}\hat{\mathbf{f}}^{(1)} - \hat{\mathbf{A}} + \hat{\mathbf{F}} + \hat{\mathbf{R}}, \tag{A.4}$$

$$\frac{\partial}{\partial t_2}\hat{\mathbf{f}}^{(0)} + \left(\frac{\partial}{\partial t_1} + +\hat{\mathbf{E}}\cdot\nabla_1\right)\hat{\mathbf{f}}^{(1)} = -\hat{\mathbf{S}}\hat{\mathbf{f}}^{(2)}, \tag{A.5}$$

with $f_i^{(k)} = O(\varepsilon^k)$, $\partial/\partial t_k = O(\varepsilon^k)$, $\partial/\partial r_{1\alpha} = O(\varepsilon)$, $A_{1i} = O(\varepsilon)$, $F_{1i} = O(\varepsilon)$, $R_{1i} = O(\varepsilon)$, $l = 1, 2, \cdots$, and $r_\alpha = x, y$. Here ε corresponds to the Knudsen number.

From Eqs. (A.3) to (A.4), we obtain

$$\frac{\partial\hat{f}_1^{eq}}{\partial t_1} + \frac{\partial\hat{f}_2^{eq}}{\partial x_1} + \frac{\partial\hat{f}_3^{eq}}{\partial y_1} = -\hat{S}_1\hat{f}_1^{(1)} + \hat{F}_1 + \hat{R}_1, \tag{A.6}$$

$$\frac{\partial\hat{f}_2^{eq}}{\partial t_1} + \frac{\partial\hat{f}_5^{eq}}{\partial x_1} + \frac{\partial\hat{f}_6^{eq}}{\partial y_1} = -\hat{S}_2\hat{f}_2^{(1)} + \hat{F}_2 + \hat{R}_2, \tag{A.7}$$

$$\frac{\partial\hat{f}_3^{eq}}{\partial t_1} + \frac{\partial\hat{f}_6^{eq}}{\partial x_1} + \frac{\partial\hat{f}_7^{eq}}{\partial y_1} = -\hat{S}_3\hat{f}_3^{(1)} + \hat{F}_3 + \hat{R}_3, \tag{A.8}$$

$$\frac{\partial\hat{f}_4^{eq}}{\partial t_1} + \frac{\partial\hat{f}_8^{eq}}{\partial x_1} + \frac{\partial\hat{f}_9^{eq}}{\partial y_1} = -\hat{S}_4\hat{f}_4^{(1)} + \hat{F}_4 + \hat{R}_4, \tag{A.9}$$

$$\frac{\partial\hat{f}_5^{eq}}{\partial t_1} + \frac{\partial\hat{f}_{10}^{eq}}{\partial x_1} + \frac{\partial\hat{f}_{11}^{eq}}{\partial y_1} = -\hat{S}_5\hat{f}_5^{(1)} + \hat{F}_5 + \hat{R}_5, \tag{A.10}$$

$$\frac{\partial\hat{f}_6^{eq}}{\partial t_1} + \frac{\partial\hat{f}_{11}^{eq}}{\partial x_1} + \frac{\partial\hat{f}_{12}^{eq}}{\partial y_1} = -\hat{S}_6\hat{f}_6^{(1)} + \hat{F}_6 + \hat{R}_6, \tag{A.11}$$

$$\frac{\partial\hat{f}_7^{eq}}{\partial t_1} + \frac{\partial\hat{f}_{12}^{eq}}{\partial x_1} + \frac{\partial\hat{f}_{13}^{eq}}{\partial y_1} = -\hat{S}_7\hat{f}_7^{(1)} + \hat{F}_7 + \hat{R}_7, \tag{A.12}$$

$$\frac{\partial\hat{f}_8^{eq}}{\partial t_1} + \frac{\partial\hat{f}_{14}^{eq}}{\partial x_1} + \frac{\partial\hat{f}_{15}^{eq}}{\partial y_1} = -\hat{S}_8\hat{f}_8^{(1)} - \hat{A}_8 + \hat{F}_8 + \hat{R}_8, \tag{A.13}$$

$$\frac{\partial\hat{f}_9^{eq}}{\partial t_1} + \frac{\partial\hat{f}_{15}^{eq}}{\partial x_1} + \frac{\partial\hat{f}_{16}^{eq}}{\partial y_1} = -\hat{S}_9\hat{f}_9^{(1)} - \hat{A}_9 + \hat{F}_9 + \hat{R}_9. \tag{A.14}$$

From Eqs. (A.3) to (A.5), we get

$$\frac{\partial\hat{f}_1^{eq}}{\partial t_2} + \frac{\partial\hat{f}_1^{(1)}}{\partial t_1} + \frac{\partial\hat{f}_2^{(1)}}{\partial x_1} + \frac{\partial\hat{f}_3^{(1)}}{\partial y_1} = -\hat{S}_1\hat{f}_1^{(2)}, \tag{A.15}$$

$$\frac{\partial\hat{f}_2^{eq}}{\partial t_2} + \frac{\partial\hat{f}_2^{(1)}}{\partial t_1} + \frac{\partial\hat{f}_5^{(1)}}{\partial x_1} + \frac{\partial\hat{f}_6^{(1)}}{\partial y_1} = -\hat{S}_2\hat{f}_2^{(2)}, \tag{A.16}$$

$$\frac{\partial\hat{f}_3^{eq}}{\partial t_2} + \frac{\partial\hat{f}_3^{(1)}}{\partial t_1} + \frac{\partial\hat{f}_6^{(1)}}{\partial x_1} + \frac{\partial\hat{f}_7^{(1)}}{\partial y_1} = -\hat{S}_3\hat{f}_3^{(2)}, \tag{A.17}$$

$$\frac{\partial\hat{f}_4^{eq}}{\partial t_2} + \frac{\partial\hat{f}_4^{(1)}}{\partial t_1} + \frac{\partial\hat{f}_8^{(1)}}{\partial x_1} + \frac{\partial\hat{f}_9^{(1)}}{\partial y_1} = -\hat{S}_4\hat{f}_4^{(2)}. \tag{A.18}$$

Adding Eqs. (A.6)–(A.9) and (A.15)–(A.18) results in the following equations,

$$\frac{\partial\hat{f}_1^{eq}}{\partial t} + \frac{\partial\hat{f}_2^{eq}}{\partial x} + \frac{\partial\hat{f}_3^{eq}}{\partial y} = \hat{F}_1 + \hat{R}_1, \tag{A.19}$$

$$\frac{\partial\hat{f}_2^{eq}}{\partial t} + \frac{\partial}{\partial x}\left(\hat{f}_5^{eq} + \hat{f}_5^{(1)}\right) + \frac{\partial}{\partial y}\left(\hat{f}_6^{eq} + \hat{f}_6^{(1)}\right) = \hat{F}_2 + \hat{R}_2, \tag{A.20}$$

$$\frac{\partial\hat{f}_3^{eq}}{\partial t} + \frac{\partial}{\partial x}\left(\hat{f}_6^{eq} + \hat{f}_6^{(1)}\right) + \frac{\partial}{\partial y}\left(\hat{f}_7^{eq} + \hat{f}_7^{(1)}\right) = \hat{F}_3 + \hat{R}_3, \tag{A.21}$$

$$\frac{\partial\hat{f}_4^{eq}}{\partial t} + \frac{\partial}{\partial x}\left(\hat{f}_8^{eq} + \hat{f}_8^{(1)}\right) + \frac{\partial}{\partial y}\left(\hat{f}_9^{eq} + \hat{f}_9^{(1)}\right) = \hat{F}_4 + \hat{R}_4. \tag{A.22}$$

Using the expressions of $\hat{f}_i^{eq}$, $\hat{F}_i^{eq}$, $\hat{R}_i^{eq}$, and Eqs. (A.10)–(A.14), we obtain the NS equations,

$$\frac{\partial\rho}{\partial t} + \frac{\partial j_\alpha}{\partial r_\alpha} = 0, \tag{A.23}$$

$$\frac{\partial j_\alpha}{\partial t} + \frac{\partial p}{\partial r_\alpha} + \frac{\partial}{\partial r_\beta}\left(\rho u_\alpha u_\beta + P_{\alpha\beta}\right) = \rho a_\alpha, \tag{A.24}$$

$$\frac{\partial\xi}{\partial t} + \frac{\partial(\xi + 2p)u_\alpha}{\partial r_\alpha} - 2\frac{\partial}{\partial r_\beta}\left[\kappa_\beta\frac{\partial T}{\partial r_\beta} - P_{\alpha\beta}u_\alpha\right] = 2\rho u_\alpha a_\alpha + 2\rho\lambda'Q, \tag{A.25}$$

where $j_\alpha = \rho u_\alpha$ is the momentum in α direction, and $\xi = (D + I)\rho T + \rho u^2$ is twice the total energy, with

$$P_{xx} = -\frac{\rho T}{\hat{S}_5}\left(2\frac{\partial u_x}{\partial x} - \frac{2}{D+I}\frac{\partial u_x}{\partial x} - \frac{2}{D+I}\frac{\partial u_y}{\partial y}\right) = \hat{f}_5^{(1)}, \tag{A.26}$$

$$P_{xy} = P_{yx} = -\frac{\rho T}{\hat{S}_6}\left(\frac{\partial u_x}{\partial y} + \frac{\partial u_y}{\partial x}\right) = \hat{f}_6^{(1)}, \tag{A.27}$$

$$P_{yy} = -\frac{\rho T}{\hat{S}_7}\left(2\frac{\partial u_y}{\partial y} - \frac{2}{D+I}\frac{\partial u_x}{\partial x} - \frac{2}{D+I}\frac{\partial u_y}{\partial y}\right) = \hat{f}_7^{(1)}, \tag{A.28}$$

$$\kappa_x = \left(\frac{D+I}{2} + 1\right)\frac{\rho T}{\hat{S}_8}, \tag{A.29}$$

$$\kappa_y = \left(\frac{D+I}{2} + 1\right)\frac{\rho T}{\hat{S}_9}, \tag{A.30}$$

which reduce to

$$P_{\alpha\beta} = -\mu\left(\frac{\partial u_\alpha}{\partial r_\beta} + \frac{\partial u_\beta}{\partial r_\alpha} - \frac{2}{3}\frac{\partial u_\chi}{\partial r_\chi}\delta_{\alpha\beta}\right) - \mu_B\frac{\partial u_\chi}{\partial r_\chi}\delta_{\alpha\beta}, \tag{A.31}$$

$$\kappa = \left(\frac{D+I}{2}+1\right)\frac{\rho T}{\hat{S}_\kappa},\qquad\qquad (A.32)$$

for $\hat{S}_5 = \hat{S}_6 = \hat{S}_7 = \hat{S}_\mu$ and $\hat{S}_8 = \hat{S}_9 = \hat{S}_\kappa$, where $\mu = \rho T/\hat{S}_\mu$ is the dynamic viscosity, $\kappa = (D+I+2)\rho T/(2\hat{S}_\kappa)$ is the thermal conductivity. With the definitions of specific heat at constant pressure $c_p = (D+I+2)/2$ and specific heat at constant volume $c_v = (D+I)/2$, we obtain the flexible specific heat ratio $\gamma = c_p/c_v = (D+I+2)/(D+I)$ and Prandtl number $Pr = c_p\mu/\kappa = \hat{S}_\kappa/\hat{S}_\mu$.

References

[1] Chu S, Majumdar A. Opportunities and challenges for a sustainable energy future. Nature 2012;488:294–303.
[2] Law CK. Combustion physics. Cambridge University Press, Cambridge; 2006.
[3] Ju Y. Recent progress and challenges in fundamental combustion research. Adv Mech 2014;44:1–72.
[4] Nagnibeda E, Kustova E. Non-equilibrium reacting gas flows: kinetic theory of transport and relaxation processes. Springer, Berlin; 2009.
[5] Succi S. The lattice Boltzmann equation for fluid dynamics and beyond. New York: Oxford University Press; 2001.
[6] Higuera FJ, Succi S, Benzi R. Lattice gas dynamics with enhanced collisions. EPL (Europhys Lett) 1989;9(4):345.
[7] Montessori A, Prestininzi P, La Rocca M, Falcucci G, Succi S. Lattice kinetic approach to non-equilibrium flows. In: AIP conference proceedings, 1738. AIP Publishing; 2016. p. 090005.
[8] Zhang Y, Qin R, Emerson DR. Lattice Boltzmann simulation of rarefied gas flows in microchannels. Phys Rev E 2005;71(4):047702.
[9] Tang GH, Zhang YH, Emerson DR. Lattice Boltzmann models for nonequilibrium gas flows. Phys Rev E 2008;77(4):046701.
[10] Meng J, Zhang Y, Shan X. Multiscale lattice Boltzmann approach to modeling gas flows. Phys Rev E 2011;83(4):046701.
[11] He X, Luo L-S. Lattice Boltzmann model for the incompressible Navier–Stokes equation. J Stat Phys 1997;88(3):927–44.
[12] Benzi R, Sbragaglia M, Succi S, Bernaschi M, Chibbaro S. Mesoscopic lattice Boltzmann modeling of soft-glassy systems: theory and simulations. J Chem Phys 2009;131(10):104903.
[13] Li Q, Luo KH, Kang Q, He Y, Chen Q, Liu Q. Lattice Boltzmann methods for multiphase flow and phase-change heat transfer. Prog Energy Combust Sci 2016;52:62–105.
[14] Lai H, Ma C. A new lattice Boltzmann model for solving the coupled viscous burgers equation. Physica A 2014;395:445–57.
[15] Schmieschek S, Narváez A, Harting J. Multi relaxation time lattice Boltzmann simulations of multiple component fluid flows in porous media. In: High performance computing in science and engineering '12. Springer; 2013. p. 39–49.
[16] Liang H, Li QX, Shi BC, Chai ZH. Lattice Boltzmann simulation of three-dimensional Rayleigh-Taylor instability. Phys Rev E 2016;93(3):033113.
[17] Ponce Dawson S, Chen S, Doolen GD. Lattice Boltzmann computations for reaction-diffusion equations. J Chem Phys 1993;98(2):1514–23.
[18] Zanette DH. Interplay of reaction and transport in a perfect fluid. Phys Rev E 1994;50(2):1171.
[19] Qian YH, Orszag SA. Scalings in diffusion-driven reaction a+b → c: numerical simulations by lattice BGK models. J Stat Phys 1995;81(1):237–53.
[20] Weimar JR, Boon JP. Nonlinear reactions advected by a flow. Physica A 1996;224(1-2):207–15.
[21] Tian Z, Xing H, Tan Y, Gu S, Golding SD. Reactive transport LBM model for CO_2 injection in fractured reservoirs. Comput Geosci 2016;86:15–22.
[22] Succi S, Bella G, Papetti F. Lattice kinetic theory for numerical combustion. J Sci Comput 1997;12:395–408.
[23] Filippova O, Hänel D. A novel numerical scheme for reactive flows at low mach numbers. Comput Phys Commun 2000;129:267–74.
[24] Yu H, Luo LS, Girimaji SS. Scalar mixing and chemical reaction simulations using lattice Boltzmann method. Int J Comput Eng Sci 2002;3:73–87.
[25] Yamamoto K, Takada N, Misawa M. Combustion simulation with lattice Boltzmann method in a three-dimensional porous structure. Proc Comb Inst 2005;30:1509–15.
[26] Lee T, Lin C, Chen LD. A lattice Boltzmann algorithm for calculation of the laminar jet diffusion flame. J Comput Phys 2006;215:133–52.
[27] Chiavazzo E, Karlin IV, Gorban AN, Boulouchos K. Efficient simulations of detailed combustion fields via the lattice Boltzmann method. Int J Numer Methods Heat Fluid Flow 2011;21:494–517.
[28] Chen S, Mi J, Liu H, Zheng C. First and second thermodynamic-law analyses of hydrogen-air counter-flow diffusion combustion in various combustion modes. Int J Hydrogen Energy 2012;37:5234–45.
[29] Succi S, Filippova O, Smith G, Kaxiras E. Applying the lattice Boltzmann equation to multiscale fluid problems. Comput Sci Eng 2001;3(6):26–37.
[30] Furtado K, Yeomans J. Lattice Boltzmann simulations of phase separation in chemically reactive binary fluids. Phys Rev E 2006;73(6):066124.
[31] Ashna M, Rahimian MH, Fakhari A. Extended lattice Boltzmann scheme for droplet combustion. Phys Rev E 2017;95(5):053301.
[32] Falcucci G, Succi S, Montessori A, Melchionna S, Prestininzi P, Barroo C, et al. Mapping reactive flow patterns in monolithic nanoporous catalysts. Microfluid Nanofluid 2016;20(7):1–13.
[33] Falcucci G, Amati G, Krastev VK, Montessori A, Yablonsky GS, Succi S. Heterogeneous catalysis in pulsed-flow reactors with nanoporous gold hollow spheres. Chem Eng Sci 2017;166:274–82.
[34] Scagliarini A, Biferale L, Mantovani F, Pivanti M, Pozzati F, Sbragaglia M, et al. Front propagation in Rayleigh-Taylor systems with reaction. In: J Phys Conf Ser, 318. IOP Publishing; 2011. p. 092024.
[35] Biferale L, Mantovani F, Sbragaglia M, Scagliarini A, Toschi F, Tripiccione R. Reactive Rayleigh-Taylor systems: front propagation and non-stationarity. EPL (Europhys Lett) 2011;94(5):54004.
[36] Chen F, Xu A, Zhang G, Li Y, Succi S. Multiple-relaxation-time lattice Boltzmann approach to compressible flows with flexible specific-heat ratio and Prandtl number. EPL (Europhys Lett) 2010;90(5):54003.
[37] Chen F, Xu A, Zhang G. Viscosity, heat conductivity, and Prandtl number effects in the rayleigh–taylor instability. Front Phys 2016;11(6):114703.
[38] Yan B, Xu A, Zhang G, Ying Y, Li H. Lattice Boltzmann model for combustion and detonation. Front Phys 2013;8(1):94–110.
[39] Lin C, Xu A, Zhang G, Li Y. Polar coordinate lattice Boltzmann kinetic modeling of detonation phenomena. Commun Theor Phys 2014;62(5):737.
[40] Lin C, Xu A, Zhang G, Li Y. Double-distribution-function discrete Boltzmann model for combustion. Combust Flame 2016;164:137–51.
[41] Xu A, Lin C, Zhang G, Li Y. Multiple-relaxation-time lattice Boltzmann kinetic model for combustion. Phys Rev E 2015;91(4):043306.
[42] Cochran SG, Chan J. Shock initiation and detonation in one and two dimensions. Lawrence Livermore National Laboratory Report; 1979. UCID–18024.
[43] Zhang Y, Xu A, Zhang G, Chen Z. Discrete Boltzmann method with maxwell–type boundary condition for slip flow. Commun Theor Phys 2018;69(1):77–85.
[44] Zhang H, Zhuang F. NND schemes and their applications to numerical simulation of two-and three-dimensional flows. Adv Appl Mech 1991;29:193–256.
[45] Watari M. Finite difference lattice Boltzmann method with arbitrary specific heat ratio applicable to supersonic flow simulations. Physica A 2007;382(2):502–22.
[46] Gan Y, Xu A, Zhang G, Li Y. Lattice Boltzmann study on Kelvin-Helmholtz instability: roles of velocity and density gradients. Phys Rev E 2011;83(5):056704.